SUPPLEMENTARY INFORMATION:

Molecular basis for allosteric regulation of RyR1 channel gating: effects of a therapeutic drug and oxidation-mimicking mutation

Jigneshkumar Dahyabhai Prajapati,[1,2,3†] Marco C Miotto[4†], Jeevan GC[5†], Haikel Dridi[4], Qi Yuan[4], Anetta Wronska[4], Yang Liu[4], Zephan Melville[4], Andrew Marks[4*], Joachim Frank[5,6*], Karissa Y. Sanbonmatsu[1,2*#]

[1]Theoretical Biology and Biophysics, Los Alamos National Laboratory, Los Alamos, New Mexico 87545, USA

[2]New Mexico Consortium, Los Alamos, New Mexico 87544, USA

[3]Department of Biological Sciences, Birla Institute of Technology and Science (BITS) Pilani, Pilani, Rajasthan, India

[4]Department of Physiology and Cellular Biophysics, Columbia University Vagelos College of Physicians and Surgeons, New York, NY 10032, USA

[5]Department of Biochemistry and Molecular Biophysics, Columbia University, New York, NY, USA

[6]Department of Biological Sciences, Columbia University, New York, NY, USA

[†]First authors

*Corresponding authors

[#]To whom correspondence may be addressed. Email: kys@lanl.gov

S1. Trajectories analysis

All trajectories were aligned to the S6 helices of RyR1 (residues E4908–C4961) prior to analysis. Analyses were performed using the PLUMED plug-in[1] patched with GROMACS v2021.4[2], together with VMD v1.9.3[3], for visualization and for generating figures and movies. ChimeraX[4] was also employed for visualization and structural analysis. Plots were generated using Gnuplot v5.4[5], and final images were refined in Inkscape v1.2.2[6].

Occupancy and coordination numbers of ligands. The coordination number (Q), which quantifies interactions between ligand atoms X and protein atoms Y within a cutoff distance (r_0) of 5 Å, was calculated as

$$Q = \sum_{i \in X} \sum_{j \in Y} \frac{1-\left(r_{ij}/r_0\right)^6}{1-\left(r_{ij}/r_0\right)^{12}},$$

where r_{ij} is the distance between ligand atom i and protein atom j[7].

Occupancy (O) was then defined as

$$O = t_{Q>0}/t,$$

the ratio of simulation time where coordination number $Q > 0$ to the total trajectory length.

To calculate residue-level occupancies, residues within 5 Å of the ligand were identified in each frame, and occupancy was reported as the fraction of frames in which a given residue was in contact with the ligand.

RY1&2 domain opening angle. The opening angle of the RY1&2 domain was calculated using vectors connecting the Cα atoms of residues L1046 to E888 ($\vec{a}$) and L1046 to V1001 ($\vec{b}$) as:

$$\phi = \cos^{-1}\left(\frac{\vec{a} \cdot \vec{b}}{|\vec{a}| \cdot |\vec{b}|}\right),$$

where $|\vec{a}|$ and $|\vec{b}|$ represent the magnitudes of the respective vectors. Only the x- and y-components of the vectors were used, so the angles represent the projection in the xy-plane.

S6 helix opening angles: The cytoplasmic side of the S6 helices (S6c) opening was quantified as the angle θ_1 between the vectors connecting the center of mass of the four hydrophobic gate residues I4937 to Cα atom of V4950 on one helix, and center-of-mass of I4937 to Cα atom of V4950 on the opposite helix. Similarly, the luminal side (S6l) opening, θ_2, was computed between the vectors connecting I4937 center-of-mass to Cα atom of V4915 on one helix and I4937 center-of-mass to Cα atom of V4915 on the opposite helix. The same procedure was applied to the remaining pair of oppositely located S6 helices to obtain all four inter-helix angles.

Channel radius profiles. The radius along the RyR1 pore axis was calculated using the HOLE program[8,9], implemented as *gmx_hole* patched with GROMACS v2018.8. For each frame of the trajectories, the pore radius was computed along the channel axis, and the average radius profile at each position was obtained by averaging over all frames across all trajectories.

Translational and rotational motions of RyR1 regions or domains. For each RyR1 domain and associated regulatory proteins (calmodulin-1 and calstabin-1) from each protomer, translational motion along the pore axis (z-axis) was calculated as the difference between the z-component of the center of mass at time t (z_t) and its initial position (z_0), then averaged over all trajectories. Positive values indicate movement away from the pore, while negative values represent movement toward the pore.

Rotational motion in the membrane plane (xy-plane) was calculated as follows: for a given domain, the angle φ was determined between two vectors: (i) one connecting the Cα atoms of I4937 in the anticlockwise and clockwise directions (cytosolic viewpoint), and (ii) the other connecting the Cα of I4937 in the clockwise direction to the domain's center of mass. Only the x- and y-components were used. The average rotational displacement was then computed as $\varphi_t - \varphi_0$ and averaged across all trajectories. Positive values indicate clockwise rotation, and negative values indicate anticlockwise rotation from the cytosolic perspective.

The same approach was taken to calculate translational and rotational motions for each RyR1 region.

Correlation analysis of RyR1 domain motions. Traditionally, correlated motions in biomolecules are assessed via dynamic cross-correlation of atomic fluctuations[10], computed as

a Pearson correlation from covariance matrix elements. In this study, we instead used center-of-mass position fluctuations of each RyR1 domain to construct the correlation matrices.

If the center-of-mass position vectors of two domains, i and j, at time t are denoted as $\boldsymbol{r}_i^t$ and $\boldsymbol{r}_j^t$, respectively, the covariance matrix element, $\bar{C}_{ij}$, is calculated as:

$$\bar{C}_{ij} = \sum_{t=1}^{N} \frac{(\boldsymbol{r}_i^t - \langle \boldsymbol{r}_i \rangle) \cdot \left(\boldsymbol{r}_j^t - \langle \boldsymbol{r}_j \rangle\right)}{N},$$

where N is the total number of frames, and $\langle \cdot \rangle$ represent the ensemble average over all frames. The normalized correlation matrix element C_{ij} is then obtained as

$$C_{ij} = \frac{\bar{C}_{ij}}{\sqrt{\bar{C}_{ii}\,\bar{C}_{jj}}}.$$

This normalization ensures that the diagonal elements equal 1, reflecting perfect self-correlation. Using the same approach, we also derived correlation matrices using only the x- and y-components of the domain COMs, which reveal correlated motions within the bilayer membrane plane. Data from all three trajectory sets were combined for each protomer to generate the final matrices.

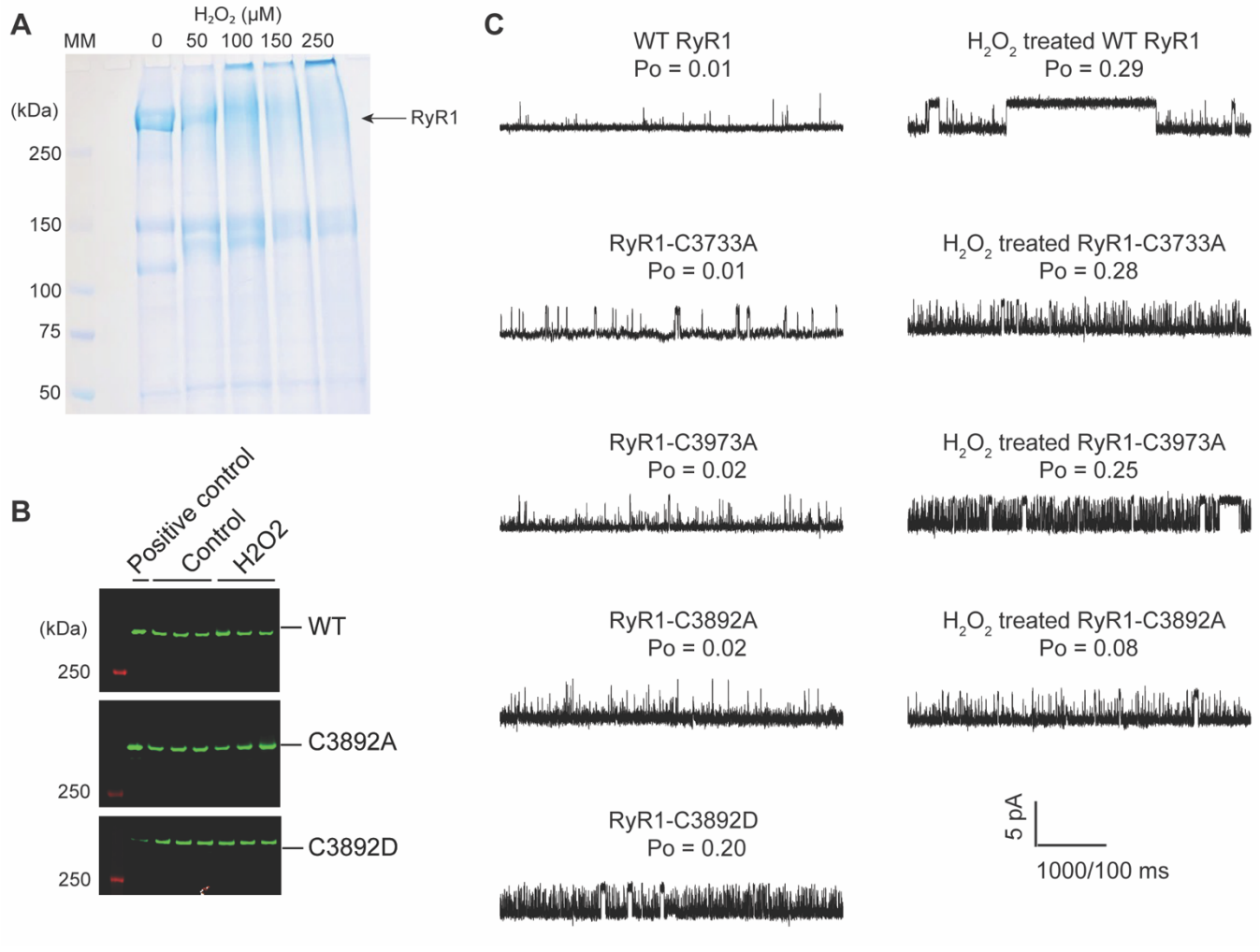


Figure S1: a) Coomassie blue-stained SDS-PAGE of RyR1 samples incubated for 30 minutes with increasing concentrations of H_2O_2 (50, 100, 150, and 250 μM) prior to immediate separation. The ~500 kDa RyR1 band is indicated by an arrow. Protein aggregation is visible in the gel wells at higher H_2O_2 concentrations. The molecular marker was loaded on the first lane. b) Western blot of HEK293 cell lysates expressing RyR1. Purified endogenous rabbit RyR1 was used as a positive control. c) Single-channel recordings of recombinantly expressed RyR1 variants: WT, C3733A, C3973A, C3892A, and C3892D, measured in the absence and presence of H_2O_2.

S2. Binding affinities of cofactors in their respective binding pockets.

Each RY1&2 domain of RyR1 can simultaneously bind one ATP and one ARM210[11]. In our simulations, ATP occupancy within the RY1&2 pocket was generally low, as the molecules frequently dissociated (Fig. 3a, main text). ATP rapidly drifted from its initial binding pose, adopting alternative poses with reduced coordination to the original interacting residues before exiting the pocket (Fig. S2a). Consistent with prior findings[11], W996 emerged as a key determinant for ATP binding, while the basic residues R886, R897, R1000, and R1020, previously suggested to contribute, were confirmed to play critical roles in stabilizing ATP interactions (Fig. S3b). Additional residues in the RY1&2 domain, including hydrophobic residues that also coordinate ARM210, were found to participate in ATP binding. ARM210 itself engaged several hydrophobic residues near W882, while also interacting with W996 and neighboring ATP-binding residues (Fig. S3a). Given the structural similarity between ATP and ARM210, and the fact that two ADP molecules occupy the same site, with one ARM210 mimicking ADP, it is plausible that ATP and ARM210 may occasionally exchange binding positions.

Within the activation core, the three cofactors (ATP, caffeine, and Ca^{2+}) exhibited markedly different binding behaviors. ATP displayed the most stable interactions, with no dissociation events observed (Fig. 3a, main text), and largely retained poses resembling its initial binding state (Fig. S2b). Ca^{2+} binding was similarly stable, maintaining near-native coordination, although occasional dissociation events were observed (Fig. 3a, main text; Fig. S2b). Notably, two of the three observed Ca^{2+} dissociation events occurred in the C3892D mutant system, located adjacent to the Ca^{2+} binding pocket, indicating weakened affinity caused by the mutation. By contrast, caffeine displayed the weakest binding, frequently dissociating from its site (Fig. S2b).

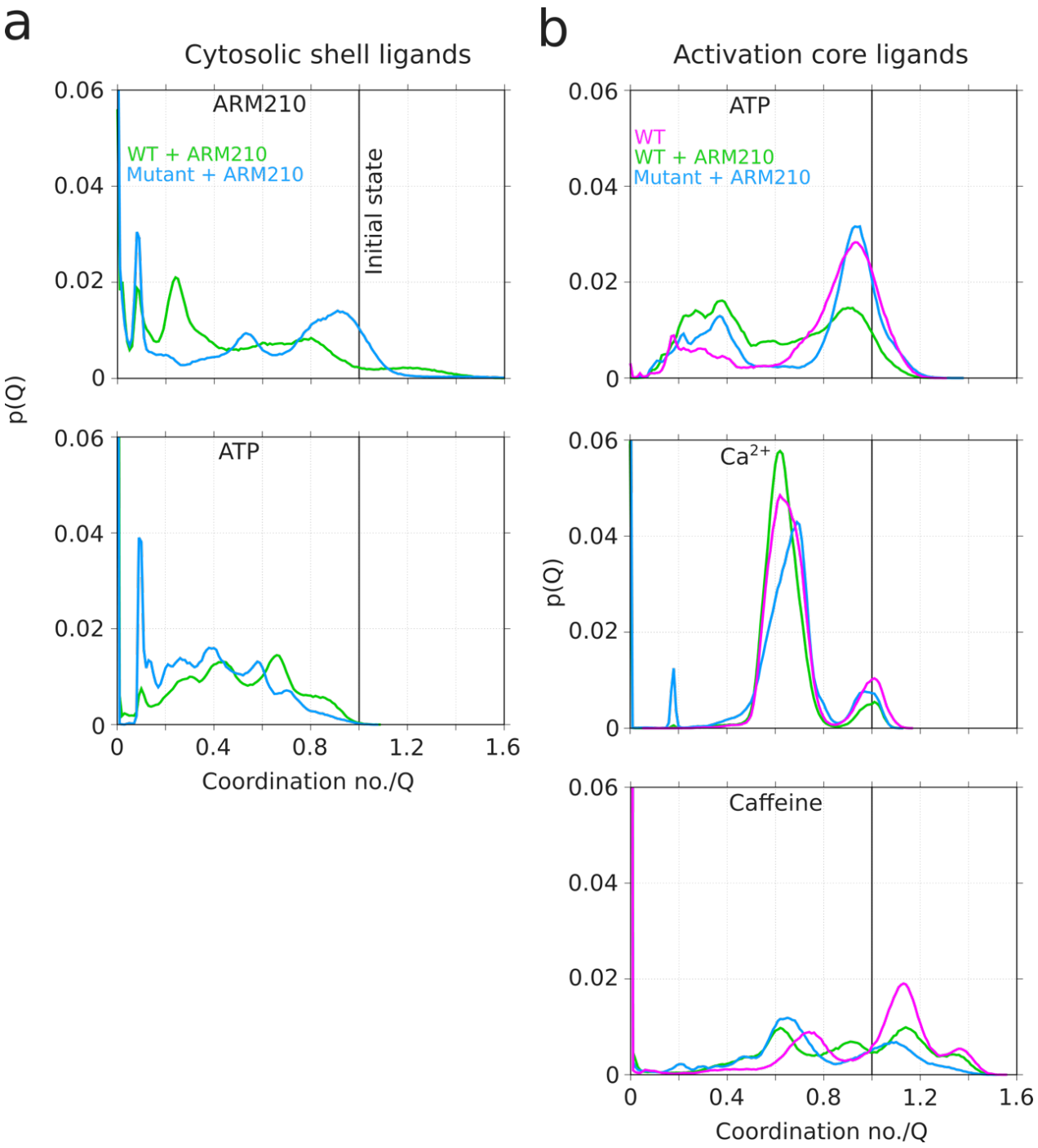


Figure S2: a) Probability distributions of the coordination number (Q) for cytosolic shell ligands interacting with binding pocket residues within 5 Å. The upper panel compares ARM210 coordination in wild-type and C3892D RyR1, while the lower panel shows ATP coordination. b) Probability distributions of the coordination number (Q) for the ligands bound to the activation core, interacting with residues within 5 Å of their binding pockets. The three panels respectively compare coordination of ATP, Ca^{2+}, and caffeine across the three simulated systems.

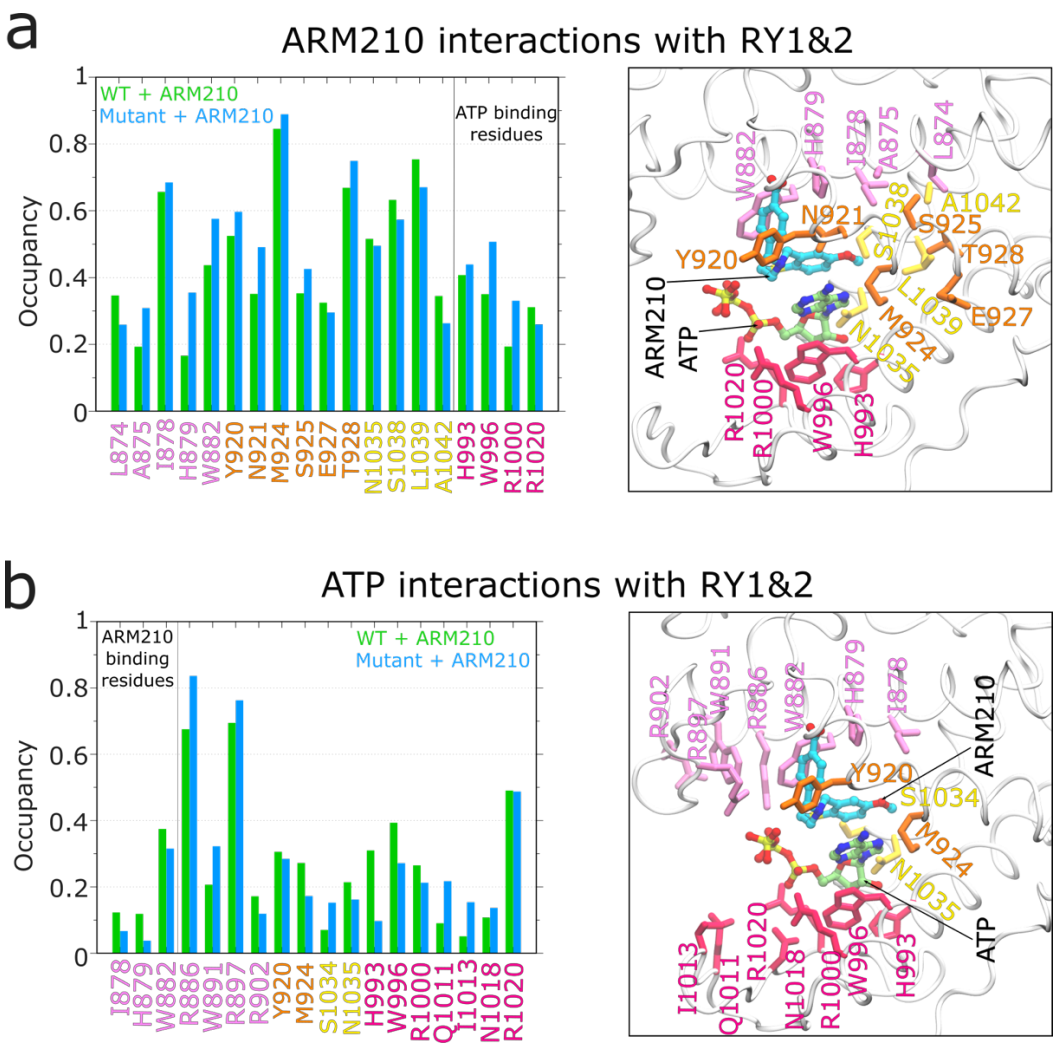


Figure S3: a) Left: Occupancy of the ARM210 molecule with residues of RY1&2 domain in wild-type and C3892D mutant RyR1, illustrating frequencies of interactions. Right: RY1&2 domain residues interacting with ARM210 are highlighted. b) Left: Occupancy of the ATP molecule RY1&2 domain resides in wild-type and C3892D mutant RyR1, illustrating interactions frequencies. Right: Residues within the RY1&2 domain interacting with ATP are shown.

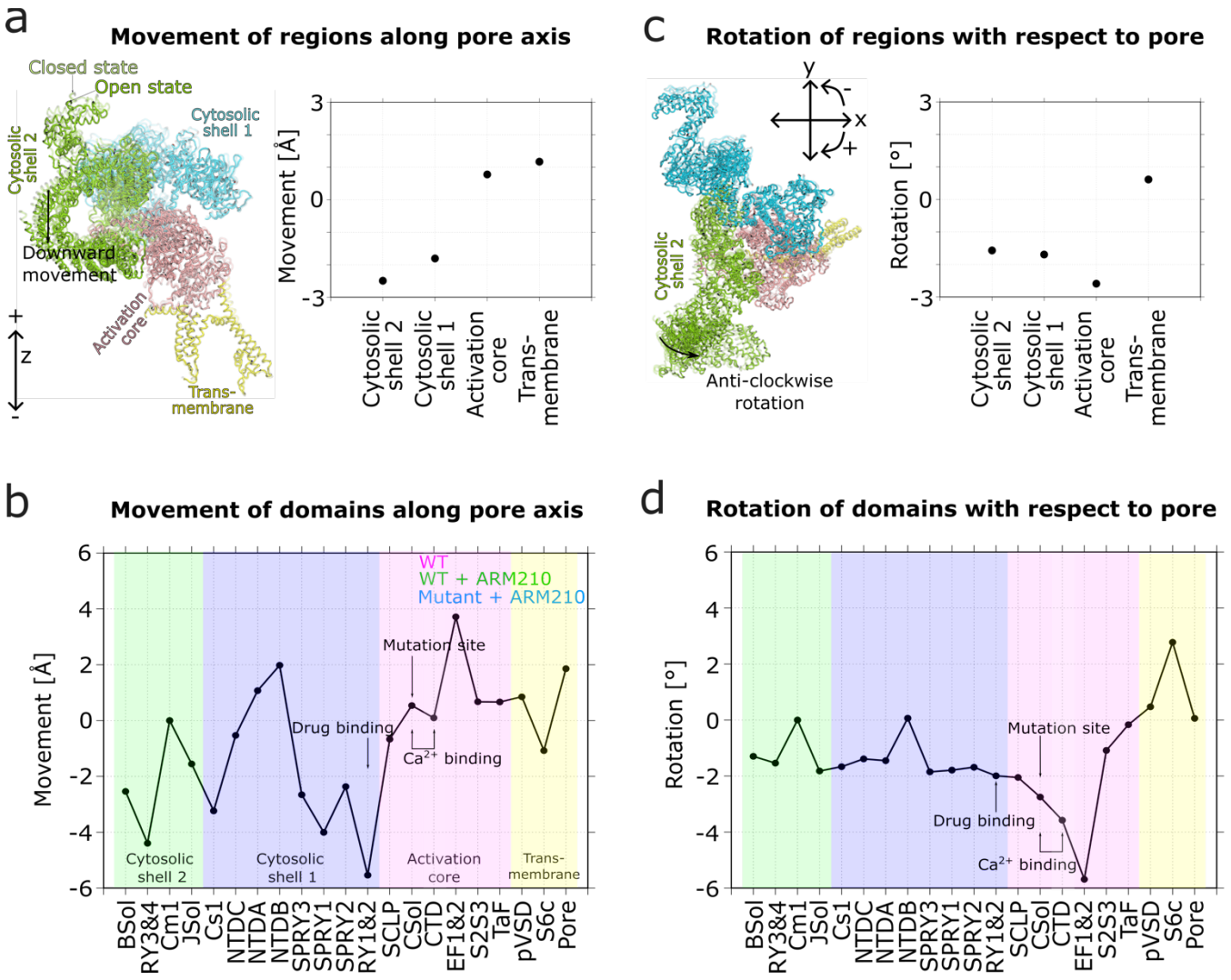


Figure S4: Translational and rotational movements of RyR1 during the transition from the closed to open state in cryo-EM structures. a) Left: Example of translational movement along the pore axis (z-axis) for the cytosolic shell 2 region, showing a downward shift ($-z$) during the closed-to-open transition (PDBs: 5TB3, 5TA3). Right: Translational movements of all four major regions in the open state relative to their initial closed-state positions (0 Å). b) Translational movements of all RyR1 domains and regulatory proteins (calmodulin-1 and calstabin-1) in the open state, referenced to the closed-state position. c) Left: Example of rotational motion of the cytosolic shell 2 region, which rotates anticlockwise in the xy-plane (negative rotation) during the closed-to-open transition. Right: Average rotational changes of all four regions relative to their initial closed-state orientation (0°). d) Rotational displacements of all RyR1 domains and regulatory proteins in the open state, relative to the closed-state orientation (0°).

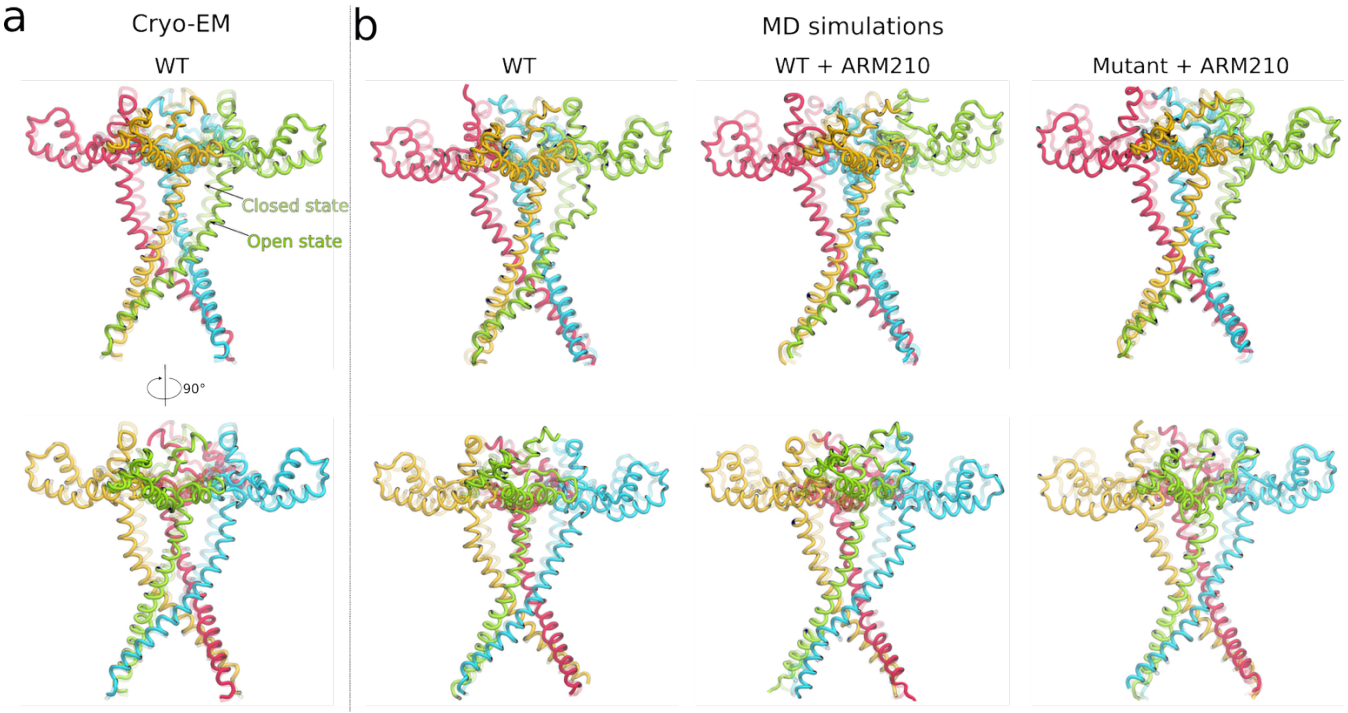


Figure S5: Opening of the S6 helices in cryo-EM structures and simulations. a) Comparison of the closed-state (translucent) with open-state (opaque) cryo-EM structures of RyR1 (PDBs: 5TB3, 5TA3), showing opening of the cytoplasmic ends of the S6 helices (S6c). b) Representative snapshots from three simulated systems comparing the initial state (translucent) with a later-stage state (opaque), illustrating a similar S6c opening as observed in the cryo-EM structures in panel (a).

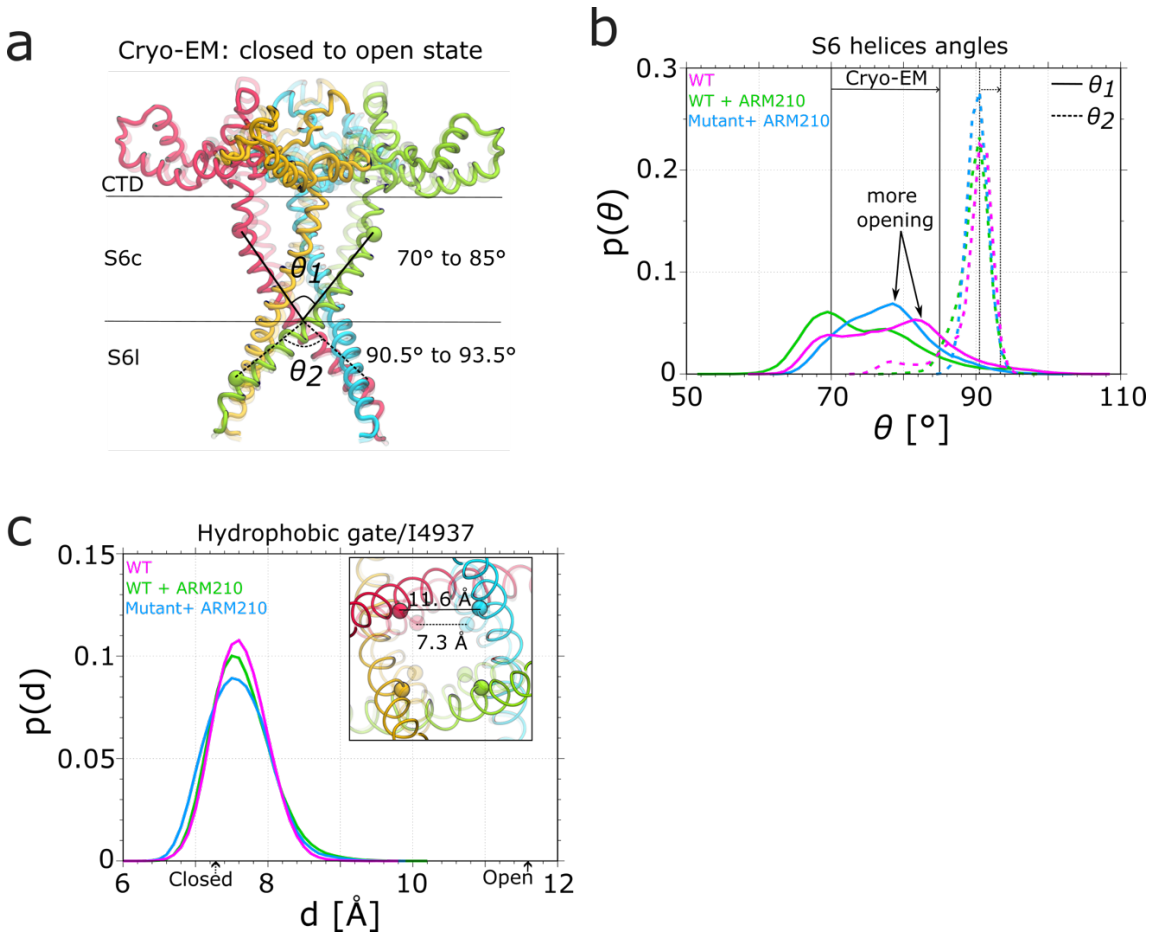


Figure S6: Structural analysis of the S6 helices in cryo-EM structures and simulations. a) Comparison of closed (translucent, PDB: 5TB3) and open (opaque, PDB: 5TA3) states of RyR1, showing opening of the cytoplasmic ends of the S6 helices (S6c) while the luminal ends (S6l) remain closed. The conformational changes are quantified by angles θ_1 (S6c) and θ_2 (S6l). b) Probability distributions of θ_1 and θ_2 across the three simulated systems, with vertical lines marking the values observed in the cryo-EM closed and open states. c) Probability distributions of the distance between C_α atoms of the hydrophobic gate residue I4937 across simulations. The inset highlights distances in the closed (7.3 Å) and open (11.6 Å) cryo-EM states. In simulations, this distance remained centered near 7.3 Å, indicating that pore dilation at the hydrophobic gate was not fully achieved, despite bending and partial opening of the S6c helices.

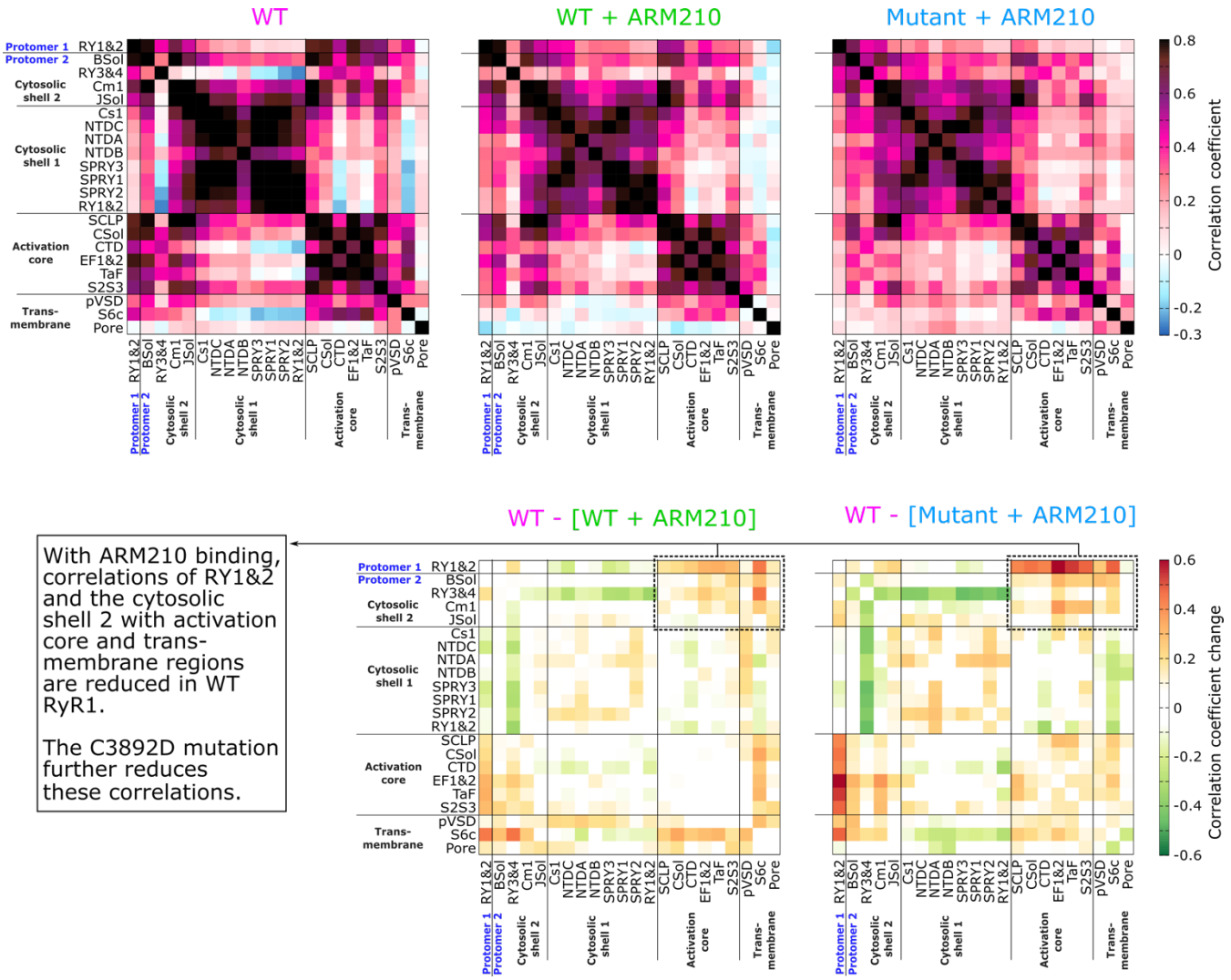


Figure S7: Top row: Same figure as panel (b) of Figure 5 in the main text. Pearson correlation coefficient matrices depicting inter-domain correlations within RyR1 and the bound regulatory proteins calmodulin-1 and calstabin-1 across the three systems. The drug-binding RY1&2 domain from the adjacent protomer (protomer 1) is also included. Bottom row: Element-wise difference matrices, representing changes in correlations for the drug-bound systems relative to the drug-free wild-type system. Larger positive or negative values indicate greater changes in correlation strength.

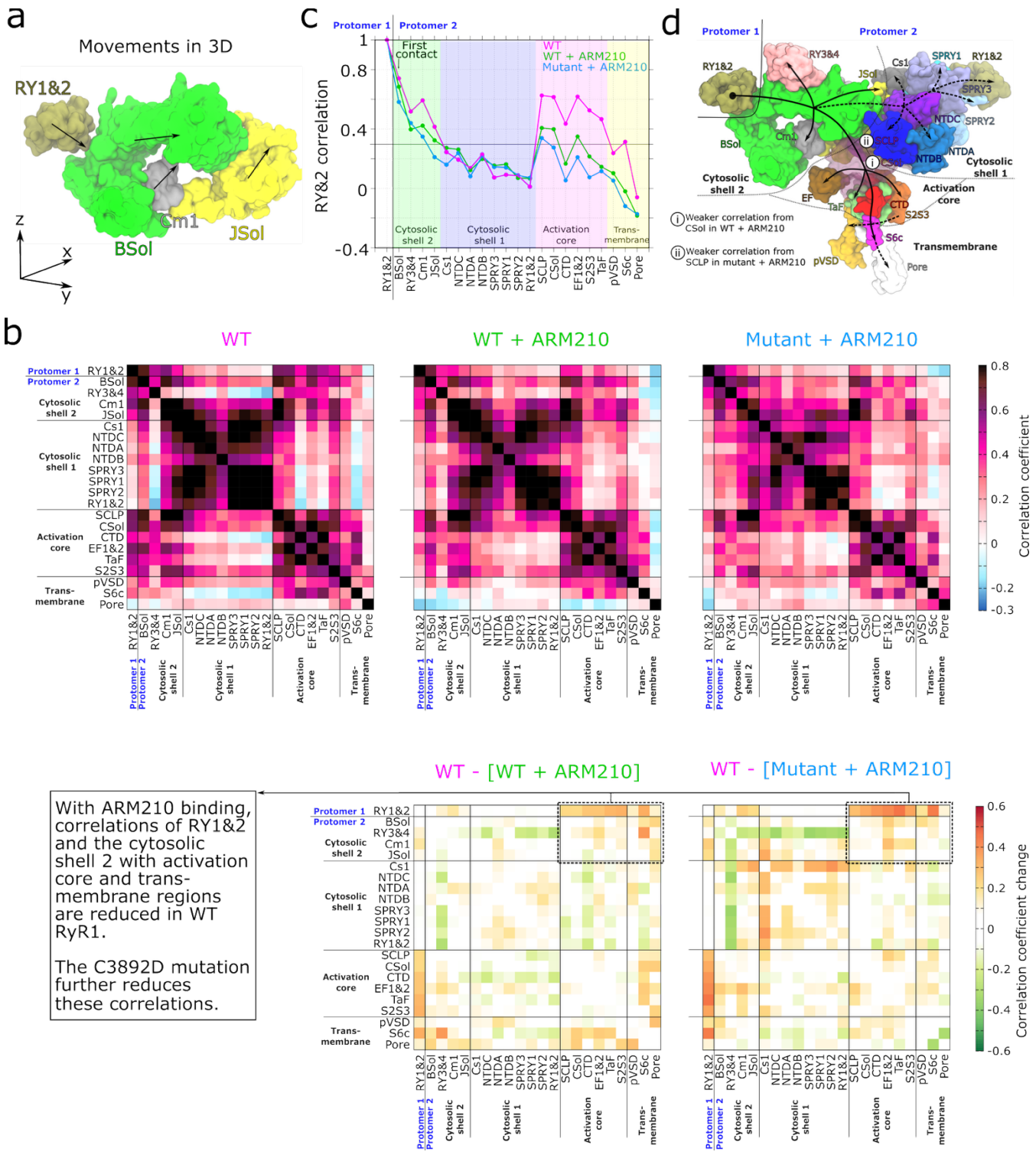


Figure S8: Correlated motions of RyR1 domains and associated regulatory proteins. a) Selected RyR1 domains are illustrated with displacement vectors representing shifts of their centers of mass in the xyz-plane relative to the initial positions. These vectors were used to compute inter-domain correlation coefficients. b) Top row: Pearson correlation coefficient matrices showing correlations among RyR1 domains and regulatory proteins (calmodulin-1 and

calstabin-1) across the three simulated systems. The drug-binding RY1&2 domain from the adjacent protomer (designated as protomer 1) is also included. Bottom row: Element-wise difference matrices, representing changes in correlations for the drug-bound systems relative to the drug-free wild-type system. Larger positive or negative values indicate greater changes in correlation strength. c) Correlation coefficients between the RY1&2 domain of protomer 1 and all other domains/regulators in protomer 2, corresponding to the first-row values from panel b, compared across the three systems. d) Network representation of correlations from panel c for the wild-type protein without drug. Solid lines denote strong correlations (> 0.3), while dotted lines indicate weaker correlations. Labels i and ii highlight domains where correlations weaken in the ARM210-bound wild-type and mutant proteins, respectively.

References

1. Tribello, G. A., Bonomi, M., Branduardi, D., Camilloni, C. & Bussi, G. PLUMED 2: new feathers for an old bird. *Comput Phys Commun* **185**, 604–613 (2014).
2. Abraham, M. J. *et al.* GROMACS: high performance molecular simulations through multi-level parallelism from laptops to supercomputers. *SoftwareX* **1–2**, 19–25 (2015).
3. Humphrey, W., Dalke, A. & Schulten, K. VMD: visual molecular dynamics. *J Mol Graph* **14**, 33–38 (1996).
4. Pettersen, E. F. *et al.* UCSF ChimeraX: structure visualization for researchers, educators, and developers. *Protein Science* **30**, 70–82 (2021).
5. Williams T, Kelley C. Gnuplot 5.4: an interactive plotting program. 2022. available from: http://www.gnuplot.info.
6. Inkscape project. Inkscape 1.2.2: draw freely. 2023. available from: https://inkscape.org.
7. White, A. D. & Voth, G. A. Efficient and minimal method to bias molecular simulations with experimental data. *J Chem Theory Comput* **10**, 3023–3030 (2014).
8. Smart, O. S., Goodfellow, J. M. & Wallace, B. A. The pore dimensions of gramicidin A. *Biophys J* **65**, 2455–2460 (1993).
9. Smart, O. S., Neduvelil, J. G., Wang, X., Wallace, B. A. & Sansom, M. S. P. HOLE: a program for the analysis of the pore dimensions of ion channel structural models. *J Mol Graph* **14**, 354–360 (1996).
10. Hünenberger, P. H., Mark, A. E. & van Gunsteren, W. F. Fluctuation and cross-correlation analysis of protein motions observed in nanosecond molecular dynamics simulations. *J Mol Biol* **252**, 492–503 (1995).
11. Melville, Z. *et al.* A drug and ATP binding site in type 1 ryanodine receptor. *Structure* **30**, 1025-1034.e4 (2022).